

PAPER

Isomorphic contact resonance force microscopy and piezoresponse force microscopy of an AlN thin film: demonstration of a new contact resonance technique

To cite this article: Lawrence H Robins *et al* 2020 *Nano Futures* 4 025003

View the [article online](#) for updates and enhancements.



PAPER

RECEIVED
24 March 2020ACCEPTED FOR PUBLICATION
27 March 2020PUBLISHED
16 June 2020

Isomorphic contact resonance force microscopy and piezoresponse force microscopy of an AlN thin film: demonstration of a new contact resonance technique

Lawrence H Robins¹ , Matt D Brubaker² , Ryan C Tung³  and Jason P Killgore¹ ¹ Applied Chemicals and Materials Division, National Institute of Standards and Technology, Boulder, CO, United States of America² Applied Physics Division, National Institute of Standards and Technology, Boulder, CO, United States of America³ Department of Mechanical Engineering, University of Nevada—Reno, Reno, NV, United States of AmericaE-mail: lawrence.robins@nist.gov and jason.killgore@nist.gov**Keywords:** atomic force microscopy, contact resonance force microscopy, piezoresponse force microscopy, piezoelectric thin film, electromechanical propertiesSupplementary material for this article is available [online](#)

Abstract

We present a new contact resonance force microscopy (CRFM) imaging technique, isomorphic contact resonance (iso-CR), that acquires data at a constant contact resonance (CR) frequency, and hence constant tip-sample contact stiffness across the scan area. Constant CR frequency is obtained by performing force versus distance measurements to vary the applied force at each pixel (i.e. force-volume mapping mode). The CR frequency increases with increasing applied force; thus, a carefully selected target frequency will be reached for most pixels at some point in the force versus distance curve. In the iso-CR mode, the cantilever maintains an invariant vibrational shape and a constant environmental damping, thus simplifying interpretation of amplitude and quality factor contrast compared to conventional CRFM. Iso-CR imaging of a piezoelectric AlN thin film sample is demonstrated. Iso-CRFM images were obtained by mechanically driving the base of the cantilever, and iso-CR piezoresponse force microscopy (iso-CR-PFM) images were obtained by electrically biasing the tip. The PFM phase images reveal that the sample contains nanoscale Al-polar (or ‘up’) and N-polar (or ‘down’) domains, with $\approx 180^\circ$ phase contrast between oppositely polarized domains. The PFM amplitude and Q-factor images also show ‘up’ vs. ‘down’ domain contrast, which decreases with increasing CR frequency. The frequency-dependent amplitude and Q contrast is ascribed to a frequency-dependent electrostatic contribution to the signal. Domain contrast is not observed in the CRFM (mechanically driven) images. To summarize, the iso-CR capability to control the resonance frequency across multiple excitation schemes helps elucidate the origin of the electromechanical and nanomechanical image contrast.

1. Introduction

Contact resonance force microscopy (CRFM) is an atomic force microscopy (AFM) method in which the tip is brought into repulsive contact with the sample, and the coupled tip-sample system is then driven at or near a mechanical resonance frequency. Analysis of the resonance characteristics, including contact force, frequency, amplitude, phase, and Q factor, can provide insight into mechanical and electromechanical sample properties [1]. Applications of CRFM to measurements of a number of material properties has been demonstrated, including elastic modulus [1, 2], viscoelasticity [3, 4], bias-induced strain due to inverse piezoelectric response [5] (piezoresponse force microscopy, PFM), and bias-induced strain due to ionic motion [6, 7] (electrochemical strain microscopy, ESM).

In most implementations of CRFM imaging, the tip is scanned over a selected sample area while maintaining a constant contact force (F_c) (as in contact-mode topographic AFM), and the resonance characteristics are measured at each pixel in the image. Well-known CRFM imaging methods include Dual

AC Resonance Tracking [8] (DART), Band Excitation [9] (BE), and Scanning Probe Resonance Image Tracking Electronics [10, 11] (SPRITE). While the contact force is held constant in these methods, the contact stiffness (k_{TS}) typically varies between pixels due to changes in tip-sample boundary conditions, such as sample modulus or tip-sample contact area (which is correlated with sample topography). The CR frequency (f_n^c , where $n \geq 1$ indicates the CR mode order) is a monotonically increasing function of k_{TS} ; hence, the pixel-scale variation of k_{TS} leads to a corresponding variation of f_n^c . These variations complicate the interpretation of CRFM image contrast, because the measured CR amplitude is proportional to a frequency dependent shape factor [12, 13], and the measured CR Q-factor is partially determined by a frequency dependent modal damping component. Thus, an observed amplitude difference between two pixels could be due to the spatial variation within the sample of some material property, or to the f_n^c dependence of the shape factor. Similarly, an observed Q-factor difference between two pixels could be due to the spatial variation within the sample of the viscoelastic loss, or to the f_n^c dependence of the modal damping.

In this work, we demonstrate a new CRFM imaging technique, denoted isomorphic CRFM (iso-CRFM), which utilizes the force-volume mapping mode of the AFM to achieve constant f_n^c for all pixels in an image, thus avoiding the problems with interpretation of image contrast in previous techniques caused by the pixel-scale variation of k_{TS} and f_n^c . In force-volume mode, the tip is initially out of contact with the sample at each pixel. The tip is moved toward the sample, contact is established, F_c is increased (extension) until a predefined maximum force is reached, F_c is then decreased (retraction), and the tip is withdrawn from contact. The tip is then moved to the next pixel and the cycle is repeated. The key concept underlying isomorphic CRFM is that k_{TS} and f_n^c increase with increasing F_c ; thus, it should be possible to reach a constant target f_n^c for some value of F_c at every pixel, provided that the maximum force is high enough. (Actually, the target f_n^c should be reached twice at each pixel, once during the extension segment of the force curve, and once during the retraction segment.) The name ‘isomorphic’ was chosen because the vibrational shape of the resonant cantilever [14, 15] is a function of f_n^c and k_{TS} ; hence, the vibrational shape is invariant provided that f_n^c and k_{TS} are constant.

To demonstrate the benefits of the iso-CR technique, iso-CRFM and iso-CR-PFM imaging results are presented for a mixed-polarity piezoelectric AlN thin-film sample that contains nanoscale up-polarity or ‘Al-polar’ and down-polarity or ‘N-polar’ domains. The polarity of this sample was previously characterized by sub-resonance (quasi-static) PFM [16]. The measured image parameters are the surface height, the amplitude, phase, and Q-factor of the resonance line, the contact force at resonance, and the adhesion force. The experimental results to be discussed include comparison of iso-CRFM (mechanically driven) and iso-CR-PFM (electrically driven) images, contrast between Al-polar and N-polar domains in iso-CR-PFM, frequency (f_n^c) dependence of iso-CR-PFM, and direct comparison of iso-CR with conventional DART-CR. The experimental results demonstrate that the ability to compare multiple excitation schemes at specific frequencies in iso-CR helps elucidate the origin of the electromechanical and nanomechanical image contrast. Furthermore, the capability to control electrostatic artifacts in PFM by tuning the CR frequency provides an additional example of the advantages of iso-CR over conventional CR.

2. Experimental procedure

2.1. Sample preparation

Epitaxial silicon-doped AlN layers (of ≈ 85 nm thickness) were grown on Si(111) substrates by molecular beam epitaxy (MBE), using a conventional effusion cell for aluminum and a radio frequency plasma source for nitrogen. The samples were grown with the goal of developing optimized N-polar and Al-polar substrates for the controlled nucleation and growth of GaN nanowires [16]. AlN layers with both polarity types were obtained by controlling the V/III ratio during MBE growth; experimental details related to synthesis can be found in [16]. The samples investigated in this study are designated D067 (mixed polarity, mostly N polar), D068 (uniform, Al polar), and D069 (uniform, N polar). (Iso-CR results for samples D068 and D069 are presented in the stacks.iop.org/NANO/F/V/A/mmedia.)

The sample polarities were previously characterized by low-frequency (i.e. $f \ll f_1^c$) PFM measurements; PFM results are shown in figure S2 (supporting information) of [16], where samples D067, D068, and D069 are labeled 5, 4, and 3, respectively. The polarity assignments based on PFM measurements were confirmed [16] in similar AlN layers by observation of polarity-dependent surface reconstructions in reflection high-energy electron diffraction (RHEED), and by polarity-dependent selective chemical etching.

Polarity control in AlN layers occurs via a polarity reversal from N- to Al-polar and appears to be mediated by incorporation of silicon impurities under N-rich growth conditions [17]. As such, the N-polar regions of the mixed-polarity sample D067 are expected to be homogenous across the entire film thickness, while the Al-polar regions likely contain an N-polar underlayer near the silicon/AlN interface.

2.2. AFM measurements

All measurements were performed with Budget Sensors ElectriTap300-G platinum-coated cantilevers¹ with the following nominal dimensions: cantilever length 125 μm , width 30 μm , thickness 4 μm , tip height 17 μm , and tip radius <25 nm. The detection laser spot was positioned at the base of the triangular picket near the cantilever tip. Calibrations based on a combination of the Sader hydrodynamic method [18, 19] and modified thermal noise method [20, 21] (GetReal¹, Oxford Instruments, Santa Barbara, CA) gave a spring constant of 24.4 N m^{-1} , inverse optical lever sensitivity of 50 nm V^{-1} , and first free resonance frequency of 283 kHz for one cantilever, which was used for most iso-CR experiments, and spring constant of 16.4 N m^{-1} , inverse optical lever sensitivity of 45.4 nm V^{-1} , and first free resonance frequency of 220 kHz for a second cantilever, which was used for the comparison of iso-CR and DART-CR.

The image size was 2 $\mu\text{m} \times 2 \mu\text{m}$ for all measurements. Most iso-CR images were acquired with a resolution of 80 \times 80 pixels (corresponding to a pixel pitch of 25 nm); one higher-resolution iso-CR image was acquired with 200 \times 200 pixels (pitch of 10 nm); and DART-CR images were acquired with 192 \times 192 pixels (pitch of 10.4 nm). The data acquisition rate was 2 pixel s^{-1} for all iso-CR measurements. (The slow acquisition rate is a limitation of the force-volume mapping mode of the AFM platform used in this work.)

The first flexural CR mode (f_1^c) was used for all measurements. For iso-CR-PFM or DART-CR-PFM imaging, an AC voltage consisting of a sum of sine waves at two drive frequencies (f_{drv1}, f_{drv2}) was applied between the tip and sample with the sample grounded; the zero-to-peak voltage at each drive frequency was set to 2 V (hence the maximum total zero-to-peak voltage was 4 V). For iso-CR-PFM, the drive frequencies were fixed at one of the following sets of values: (1085 kHz, 1095 kHz), (1095 kHz, 1105 kHz), (1105 kHz, 1115 kHz), (1125 kHz, 1135 kHz), or (1077 kHz, 1085 kHz), corresponding to target CR frequencies (f_1^c) of 1090 kHz, 1100 kHz, 1110 kHz, 1130 kHz, or 1081 kHz. For both DART-CR-PFM and DART-CRFM, the drive frequencies were varied in a manner controlled by the DART feedback loop, with fixed difference $f_{drv2} - f_{drv1} = 8 \text{ kHz}$.

For iso-CRFM or DART-CRFM imaging, the cantilever was mechanically (photothermally) excited by a 405 nm laser with the light spot positioned near the base of the cantilever (where the cantilever is attached to the supporting chip), and the laser intensity was modulated to create an AC component consisting of a sum of sine waves at two drive frequencies (f_{drv1}, f_{drv2}); the AC optical power at each drive frequency was set to 0.5 mW. For iso-CRFM, the drive frequencies were fixed at one of the following sets of values: (1065 kHz, 1075 kHz), (1085 kHz, 1095 kHz), (1105 kHz, 1115 kHz), or (1077 kHz, 1085 kHz), corresponding to target CR frequencies (f_1^c) of 1070 kHz, 1090 kHz, 1110 kHz, or 1081 kHz.

The maximum F_c (the force at which the cantilever motion changes from extension to retraction) was 610 nN for most iso-CR measurements of sample D067. In the comparative measurements of iso-CR and DART-CR, the maximum F_c for iso-CR was 1500 nN, while the fixed F_c for DART-CR was 750 nN. The maximum F_c was 1500 nN for iso-CR measurements of samples D068 and D069 (supplementary data). Note that the high F_c values attained in this work, which are advantageous for iso-CR, were enabled by the use of relatively high spring constant (16.4 N m^{-1} or 24.4 N m^{-1}) cantilevers.

3. Isomorphic contact resonance: methodology

3.1. Modeling and data analysis

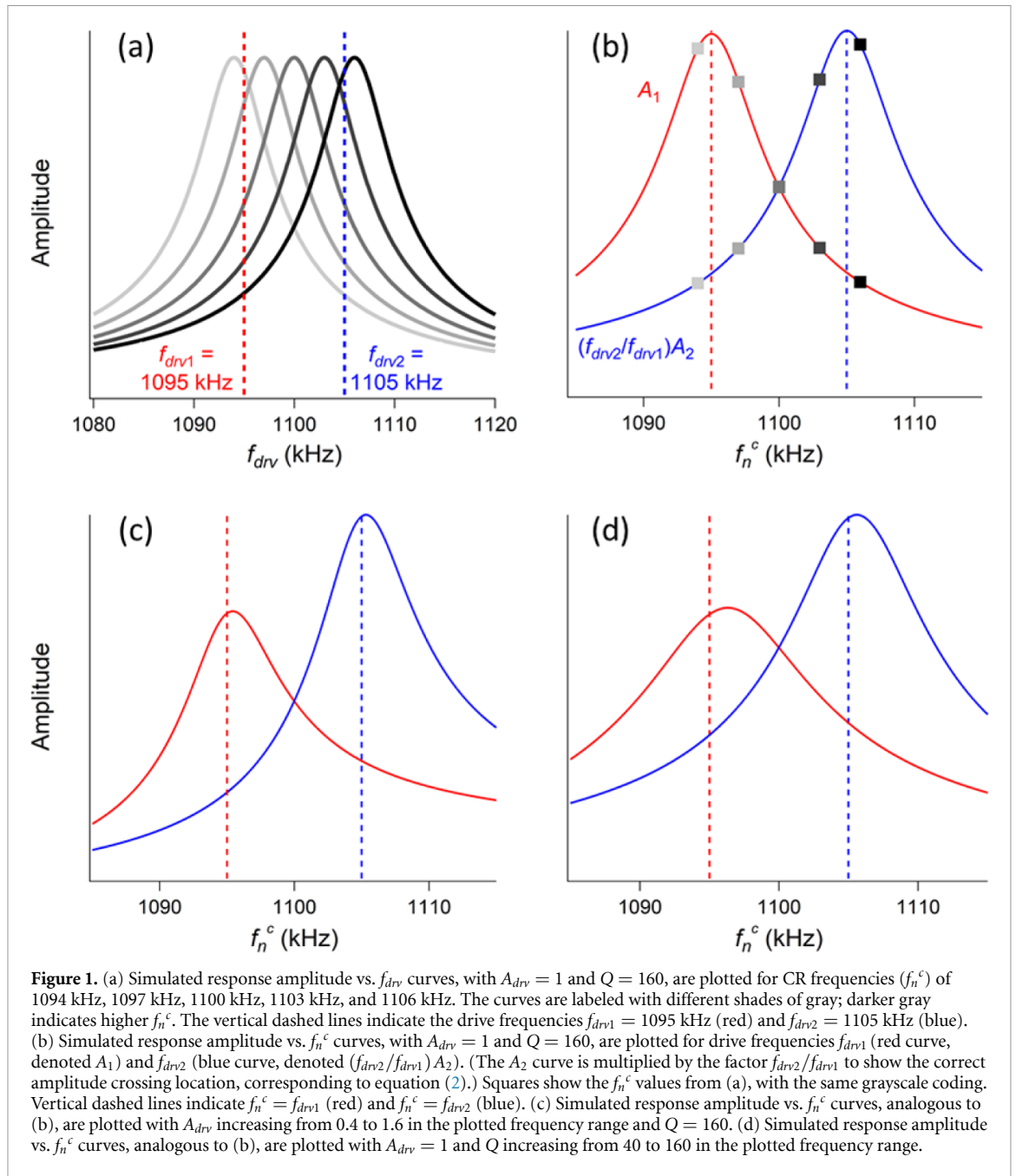
The experimental implementation of iso-CR is conceptually described here. In the DHO model (see equation (1) of [8]), the dependence of the response amplitude $A(f_{drv}, f_n^c)$ on the drive frequency f_{drv} and the CR frequency f_n^c is given by

$$A(f_{drv}, f_n^c) = \frac{(f_n^c)^2 A_{drv}(f_n^c) Q(f_n^c)}{\sqrt{[Q(f_n^c) (f_{drv}^2 - (f_n^c)^2)]^2 + [f_n^c \cdot f_{drv}]^2}}, \quad (1)$$

where f_n^c increases monotonically with F_c and can thus be experimentally controlled by varying F_c , and the drive amplitude A_{drv} and quality factor Q are functions of f_n^c .

Two methods for probing the frequency dependence of $A(f_{drv}, f_n^c)$ are shown schematically in figure 1. In the first method, f_{drv} is varied continuously within some range, for one or more discrete values of F_c and hence f_n^c , as shown in figure 1(a). The five response amplitude curves in figure 1(a) correspond to f_n^c of

¹ Commercial equipment, instruments, or materials are identified only in order to adequately specify certain procedures. In no case does such identification imply recommendation or endorsement by the National Institute of Standards and Technology, nor does it imply that the products identified are necessarily the best available for the purpose.



1094 kHz, 1097 kHz, 1100 kHz, 1103 kHz, and 1106 kHz, with constant $A_{drv} = 1$ and $Q = 160$ (similar to the highest Q observed experimentally in this work). For each curve, the peak amplitude corresponds to $f_{drv} = f_n^c$. The vertical dashed lines in figure 1(a) mark the response amplitudes at two drive frequencies, $f_{drv1} = 1095$ kHz and $f_{drv2} = 1105$ kHz. The response amplitudes at f_{drv1} and f_{drv2} are seen to be (approximately) equal for the $f_n^c = 1100$ kHz curve, i.e. when f_n^c is midway between f_{drv1} and f_{drv2} .

The method of figure 1(a) is commonly used for quantifying f_n^c in single-point CRFM (with the tip at a fixed location on the sample). However, in an imaging experiment, the dependence of f_n^c on F_c varies from pixel to pixel. Hence, imaging based on this method with a fixed set of F_c values will, in general, result in different f_n^c values at each pixel. This is inconsistent with the iso-CR goal of keeping f_n^c constant. In addition, the data acquisition rate for an imaging method based on acquisition of several f_{drv} ‘sweeps’ (for different values of F_c) at each pixel would be impractically slow—much slower than even the 2 pixel s^{-1} rate of the iso-CR method presented in this work.

The second method, shown in figures 1(b)–(d), is derived from force-volume mapping mode. In this method, F_c and hence f_n^c is varied continuously within some range, while the tip-sample contact is simultaneously driven at two discrete frequencies, f_{drv1} and f_{drv2} . The response amplitudes at f_{drv1} and f_{drv2} ,

denoted A_1 and A_2 respectively, are measured as functions of F_c . (In figures 1(b)–(d), it is assumed for simplicity that f_n^c is a known function of F_c , hence f_n^c rather than F_c is plotted on the x-axis.)

The iso-CR experiments in this work are based on the method of figures 1(b)–(d). The following relation, which is derived from equation (1), shows how this method enables acquiring data at constant f_n^c :

$$\text{if } f_n^c = \sqrt{f_{drv1}f_{drv2}} \text{ then } A_1(f_n^c) = (f_{drv2}/f_{drv1}) A_2(f_n^c). \quad (2)$$

The CR frequency f_n^c has the fixed value $f_{target} \equiv \sqrt{f_{drv1}f_{drv2}}$ at the ‘amplitude crossing point’ $A_1 = (f_{drv2}/f_{drv1}) A_2$. Hence, identifying the amplitude crossing point at each pixel fulfills the iso-CR requirement. (The response amplitudes A_1 and $(f_{drv2}/f_{drv1}) A_2$ are plotted in figures 1(b)–(d), rather than A_1 and A_2 , to correctly locate the crossing point.)

It is typical in CRFM that A_{drv} and Q vary with f_n^c due to non-constant ‘shape factor’ and modal damping. Comparison of figures 1(b)–(d) illustrates the effect of different dependencies of A_{drv} and Q on f_n^c . In figure 1(b), A_{drv} and Q are constant, with the same values as in figure 1(a). Therefore, $f_n^c = f_{drv1}$ at the maximum of the A_1 curve, and $f_n^c = f_{drv2}$ at the maximum of the A_2 curve. In figure 1(c), A_{drv} increases linearly from 0.4 to 1.6 within the plotted f_n^c range, while Q is constant. In figure 1(d), Q increases linearly from 40 to 160 within the plotted f_n^c range, while A_{drv} is constant. It is seen that when either A_{drv} or Q has a non-zero slope vs. f_n^c , the maxima of the amplitude curves are displaced from the ‘CR frequency = drive frequency’ points (the red and blue vertical dashed lines) and do not correspond to known frequencies; hence these maxima are not accurate indicators for iso-CR. In addition, figures 1(c) and (d) confirm that the amplitude crossing condition of equation (2) holds when A_{drv} or Q is frequency-dependent.

To fully determine the fit parameters in the DHO model (A_{drv} , Q , and drive phase φ_{drv}), the phase shifts with respect to the drive signals at frequencies f_{drv1} and f_{drv2} , φ_1 and φ_2 , are measured in addition to the response amplitudes A_1 and A_2 . The fit parameters are then calculated from A_1 , A_2 , φ_1 , and φ_2 based on [8], with $f_n^c = f_{target}$:

$$A_{drv} = A_1 \left(1 - \frac{f_{drv1}}{f_{drv2}} \right) \sqrt{1 + \frac{1}{X_1^2}}, \quad (3)$$

$$\varphi_{drv} = \varphi_1 - \tan^{-1} \left\{ |X_1|^{-1} \right\}, \quad (4)$$

$$\text{and } Q = \left(\frac{f_n^c}{f_{drv2} - f_{drv1}} \right) |X_1|, \quad (5)$$

where X_1 is defined as

$$X_1 = -\frac{1 - \text{sgn}(\Phi) \sqrt{1 + \Phi^2}}{\Phi}, \text{ with, } \Phi = \tan(\varphi_2 - \varphi_1). \quad (6)$$

3.2. Comparison of iso-CR and DART

The new iso-CR method presented here has several similarities to the well-known [8] DART-CR method. Both methods are based on driving the tip-sample system with a sum of sine waves at two frequencies f_{drv1} and f_{drv2} , and finding a resonance frequency (f_n^c) midway between the drive frequencies from an amplitude matching condition. Key differences are as follows.

In DART, F_c is held constant, while k_{TS} and f_n^c vary between pixels. The first drive frequency f_{drv1} (and thus the average drive frequency $0.5(f_{drv1} + f_{drv2})$) is continually adjusted by a feedback loop (with $f_{drv2} - f_{drv1}$ fixed) to maintain equality of the amplitudes A_1 and A_2 and hence track f_n^c , based on an approximation to equation (2),

$$\text{if } f_n^c = 0.5(f_{drv1} + f_{drv2}) \text{ then } A_1(f_n^c) = A_2(f_n^c), \quad (7)$$

which is valid when $f_{drv2} - f_{drv1} \ll f_n^c$. (Use of this approximation simplifies design of the DART feedback loop that provides the required frequency tracking.)

In iso-CR, F_c is varied between zero and a pre-selected maximum at each pixel, with f_{drv1} and f_{drv2} held constant. In contrast to DART, no feedback loop is needed. Complete amplitude (A_1 , A_2) and phase (φ_1 , φ_2) vs. force curves are recorded and saved. The force point that satisfies the amplitude-crossing condition of equation (2) is located in post-acquisition data analysis, and the DHO model parameters at the ‘crossing force’ are then calculated from equations (2)–(6).

3.3. Advantages of iso-CR over standard CRFM methods

Iso-CR offers several advantages over standard CRFM methods (including DART and band excitation) that are based on imaging with constant F_c and variable f_n^c . In particular, iso-CR provides a more direct path to quantification of important material properties, as explained below.

- (a) Quantification of bias-induced strain in PFM and ESM requires knowledge of the ‘shape factor’ that gives the ratio of the cantilever deflection to the vertical tip displacement [12, 13]. The shape factor is determined by the vibrational shape of the cantilever and the laser spot position on the cantilever. In iso-CR, the vibrational shape is invariant and hence the shape factor is constant. Thus, the deflection amplitude image is directly proportional to the tip displacement image; i.e. the ratio of the measured deflection amplitudes at any two pixels is equal to the ratio of the tip displacements. On the other hand, in standard CRFM, the shape factor varies from pixel to pixel, and errors in determination of the shape factor may result in a distorted tip displacement image; significant errors are likely to occur at frequencies near anti-nodes (where the shape factor approaches zero).
- (b) A ‘sensitivity factor’ for CR-PFM and CR-ESM is defined [12, 13] as the product of the shape factor and Q ; the sensitivity factor describes the ratio of the measured deflection signal at the resonance peak to the tip displacement. In iso-CR, f_n^c can be tuned to maximize the sensitivity factor and hence the signal-to-noise ratio for the entire image. In standard CRFM, the sensitivity factor may be high in some parts of the image and low in other parts.
- (c) The interpretation of Q is simplified by operation at constant frequency. The total measured damping ($1/Q$) can be described as a sum of a sample damping term $1/Q_S$ due to viscoelastic loss, and a modal damping term $1/Q_{modal}$ due to damping of the cantilever motion in air (or other surrounding medium), which is affected by the vibrational shape of the cantilever and the proximity of the sample surface. Both damping terms are, in general, functions of frequency:

$$\frac{1}{Q} = \frac{1}{Q_S(f_n^c)} + \frac{1}{Q_{modal}(f_n^c)}, \quad (8)$$

In iso-CR, f_n^c and $Q_{modal}(f_n^c)$ are constant; thus, any image contrast in Q can be attributed to inhomogeneity in the material properties that determine viscoelastic loss (at a fixed value of f_n^c) or, as discussed later, variations in the AC drive force. Further, images can be acquired at different values of f_n^c , providing information on the frequency dependence of the viscoelastic loss. In standard CRFM, due to the pixel-to-pixel variation of f_n^c , Q image contrast may arise from the frequency dependence of the modal damping, the frequency dependence of the viscoelastic loss, or inhomogeneous viscoelastic loss at fixed frequency. The multiple possible mechanisms for the image contrast complicate the interpretation of the data.

- (d) The sample indentation modulus can be calculated from CR measurements via a Hertzian contact model, which assumes indentation of a flat surface by a hemispherical tip. According to the Hertzian model (see equations (4.8)–(4.12) of [1]), the vertical tip-sample contact stiffness is

$$k_{TS} = 2 \left(\frac{3}{4} R F_t \right)^{\frac{1}{3}} (E^*)^{\frac{2}{3}}, \quad (9)$$

where R is the tip radius of curvature, F_t is the total tip-sample contact force ($F_t = F_c + F_{adh}$ where F_c is the applied contact force and F_{adh} is the adhesion force), and E^* is the reduced tip-sample modulus given by

$$\frac{1}{E^*} = \frac{1}{M_S} + \frac{1}{M_T}, \quad (10)$$

where M_S and M_T are respectively the sample and tip indentation modulus. In iso-CR imaging with constant k_{TS} , the ratio of reduced moduli at two pixels (denoted p_1 and p_2) is given by

$$\frac{E^*(p_2)}{E^*(p_1)} = \left(\frac{F_t(p_1)}{F_t(p_2)} \right)^{0.5}. \quad (11)$$

Because of the incorporation of force-volume mapping with iso-CRFM, the adhesion force F_{adh} is quantified, and hence F_t is known. Thus, when appropriate (e.g. for adhesion forces acting primarily outside the contact zone), the Hertz analysis can be modified to be Derjaguin-Müller-Toporov—like. Further, when calculating a

ratio of forces in AFM, the calibration factor relating force to photodetector voltage cancels; thus, the modulus ratio of equation (11) depends only on a ratio of photodetector voltages. In standard CRFM, the reduced modulus ratio is given by

$$\frac{E^*(p_2)}{E^*(p_1)} = \left(\frac{F_t(p_1)}{F_t(p_2)} \right)^{0.5} \left[\frac{k_{TS}(f_n^c(p_2))}{k_{TS}(f_n^c(p_1))} \right]^{1.5}, \quad (12)$$

where the CR frequencies $f_n^c(p_1)$ and $f_n^c(p_2)$ are measured, but the functional dependence of k_{TS} on f_n^c is sensitive to details of the cantilever geometry. Hence, imperfect modeling of the cantilever by the beam model used for analysis may lead to errors in the calculation of $k_{TS}(f_n^c)$. In addition, F_{adh} is not typically measured in standard CRFM, hence F_t is not fully determined. (It is possible to perform standard CRFM in force-volume mapping mode, enabling measurement of F_{adh} .)

Note that variation of the tip-sample contact area due to surface topography is not accounted for in the Hertzian model (which assumes a flat surface), and may lead to topography-related artifacts in the F_t (iso-CR) or f_n^c (standard CRFM) image contrast. In addition, any change in R due to tip damage during data acquisition will affect the modulus measurements. These problems are not solved by iso-CR.

- (e) In the DART method, if the frequency tracking mechanism fails at one pixel, possibly due to low response amplitude or an abrupt change in f_0 , often the tracking will not be restored at later pixels, hence data will not be obtained at the later pixels [15]. For example, after a large change in f_n^c , such that f_n^c is not bounded by the current drive frequencies f_{drv1} and f_{drv2} at the new pixel, the frequency tracking may not be recoverable because the response amplitudes A_1 and A_2 are too small to provide the needed input to the DART feedback circuit. Because iso-CR uses a non-tracking method of data acquisition, a measurement failure at one pixel does not affect subsequent pixels. Further, the frequency tracking in DART is imperfect due to the non-zero feedback time constant(s), i.e. a tracking error $(0.5(f_{drv1} + f_{drv2}) - f_n^c)$ can be defined at each pixel. The effect of tracking error on measurements of the fit parameters was recently analyzed in the context of DART-CR-PFM and DART-CR-ESM experiments [22]. Frequency tracking error does not occur in iso-CR because the drive frequencies are fixed.
- (f) Standard CRFM is usually performed in contact mode, in which the tip is moved laterally while in contact with the sample, and shear tip-sample forces are present. In the force-volume mapping mode used for iso-CR, shear forces are avoided, thus reducing tip and sample damage as compared to contact mode.

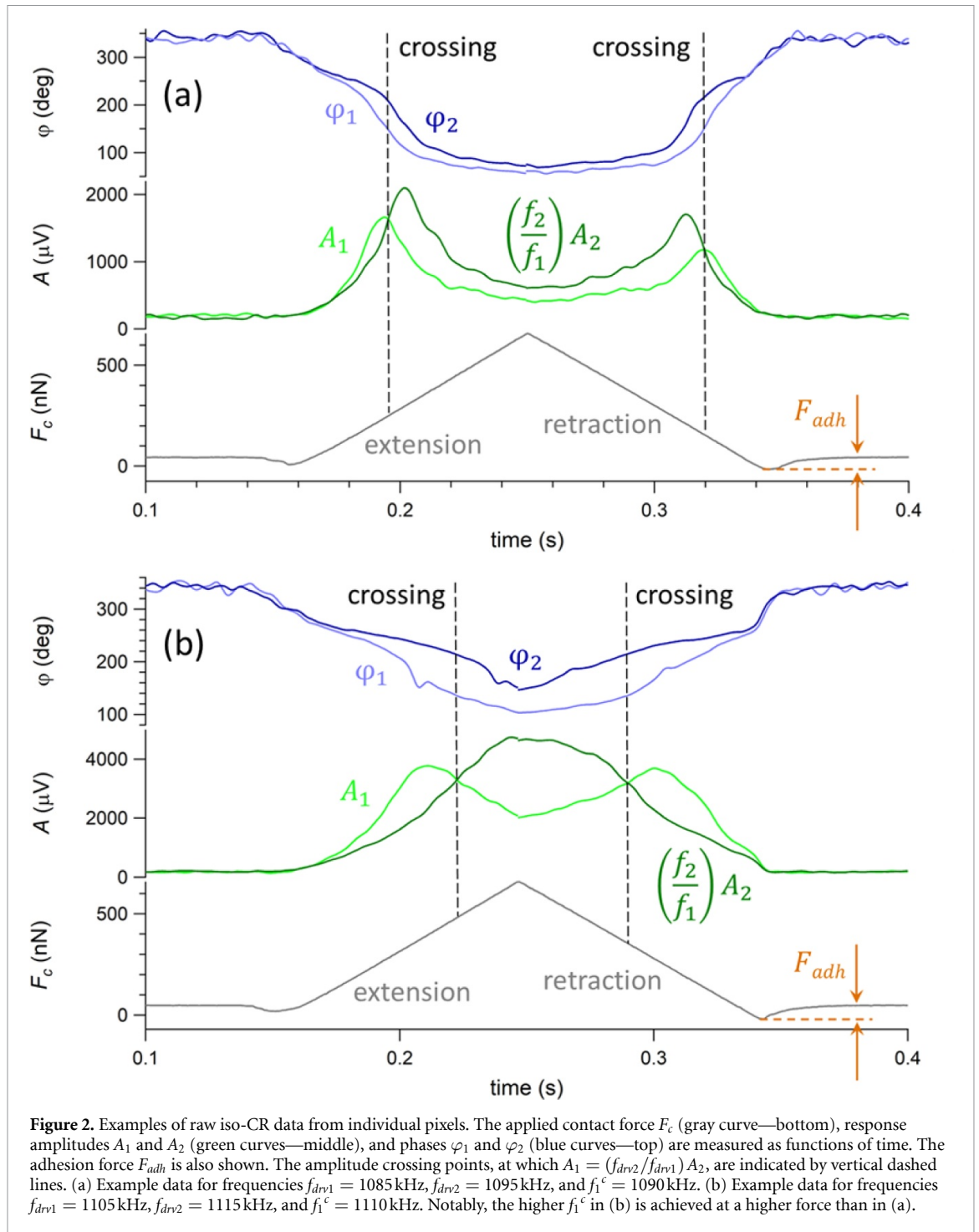
4. Experimental results

4.1. Examples of raw iso-CR data

Examples of raw (as-measured) iso-CR data from individual pixels are shown in figure 2(a), for frequencies $f_{drv1} = 1085$ kHz, $f_{drv2} = 1095$ kHz, and $f_1^c = 1090$ kHz, and figure 2(b), for frequencies $f_{drv1} = 1105$ kHz, $f_{drv2} = 1115$ kHz, and $f_1^c = 1110$ kHz. (Note that the pixels represented in figures 2(a) and (b) are distinct and well-separated. The 1st flexural CR mode ($n = 1$) was used for all experiments.) In figures 2(a) and (b), all parameters are plotted as functions of time during the extension and retraction segments of the force curve; the lower plot shows the contact force, the middle plot shows the response amplitudes A_1 and $(f_{drv2}/f_{drv1})A_2$, and the upper plot shows the phases φ_1 and φ_2 . (The z coordinate of the tip piezo stage, not shown, increases linearly with time during the extension segment and decreases linearly with time during the retraction segment.) The amplitude crossing points, at which $A_1 = (f_{drv2}/f_{drv1})A_2$ and hence $f_1^c = \sqrt{f_{drv1}f_{drv2}}$, are indicated by vertical dashed lines. The adhesion force, defined as the difference between the force measured after the tip is pulled off the sample (which is effectively zero force) and the minimum force at the pull-off point, is also illustrated in figure 2. Intuitively, the crossing force for $f_1^c = 1110$ kHz is greater than for $f_1^c = 1090$ kHz because the higher force corresponds with higher k_{ts} . Correspondingly, at a fixed f_1^c a stiffer material will exhibit crossing at a lower force. At crossing, the phase difference is larger for $f_1^c = 1110$ kHz than for $f_1^c = 1090$ kHz, indicating a higher Q value for the resonance.

4.2. Iso-CR imaging with electrical and mechanical excitation

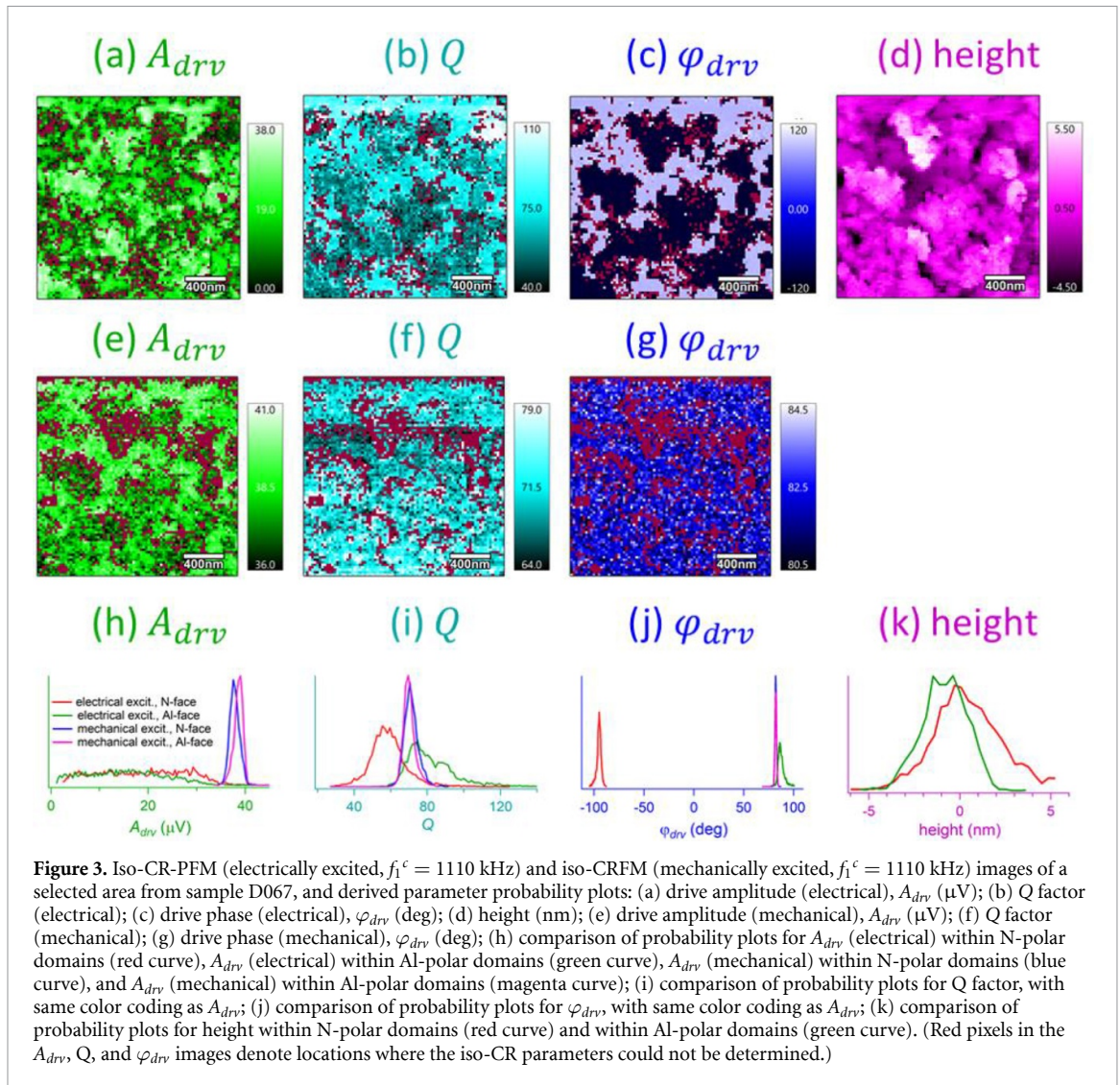
Iso-CR imaging results, for electrical or mechanical excitation with $f_1^c = 1110$ kHz, are shown in figure 3. The displayed parameters are drive amplitude (A_{drv}) (first column), Q factor (Q) (second column), drive phase (φ_{drv}) (third column), and surface height (fourth column). The parameters are color-coded as follows: green for A_{drv} , cyan for Q , blue for φ_{drv} , and magenta for height. The first row (figures 3(a)–(d)) shows images obtained with electrical excitation, the second row (figures 3(e)–(g)) shows images obtained with mechanical (photothermal) excitation, and the third row (figures 3(h)–(k)) shows comparative probability plots of the results. Note that the color (light to dark) scales are different for the electrically and mechanically excited



images. The color scale for each image is chosen to facilitate visualization of the contrast within the given image. To compare the parameter values for electrical and mechanical excitation, see the probability plots.

The red regions in the amplitude, Q , and phase images represent pixels where the iso-CR parameters were not determined because a unique amplitude crossing could not be identified; these pixels are excluded from the data analysis. Examination of the raw data showed that failure to find a unique amplitude crossing is usually due to either low drive amplitude and hence poor signal-to-noise (if the amplitude signals are noisy, there will typically be several ‘false crossings’ of the A_1 and $(f_{drv2}/f_{drv1})A_2$ curves) or insufficient contact force (such that the amplitude crossing is never reached within the force range of the experiment).

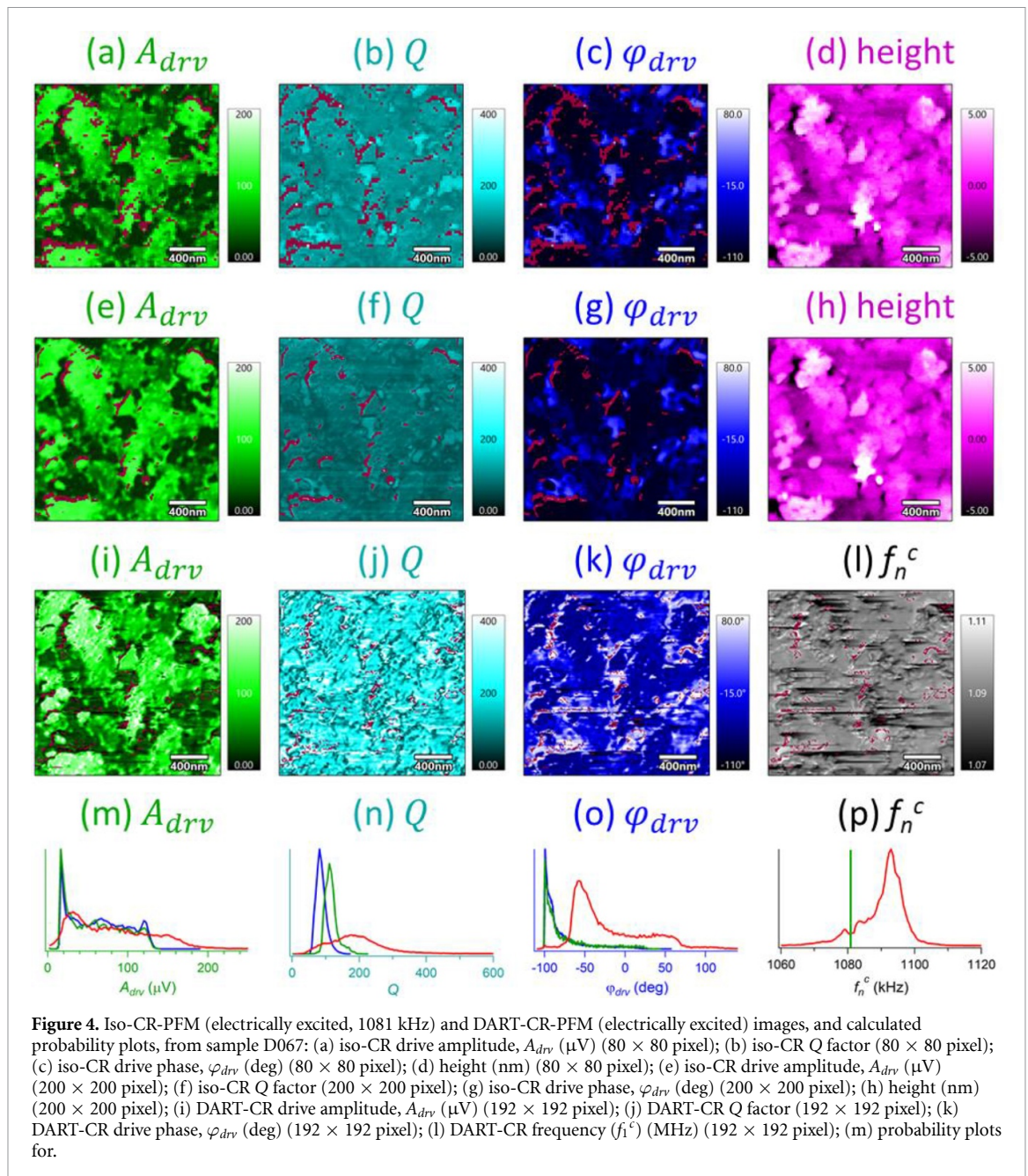
The electrically driven phase image (figure 3(c)) has a strongly bimodal character, with distinct ‘low phase’ and ‘high phase’ regions with values of φ_{drive} are near -95° and 86° respectively. (Note that φ_{drive} was not corrected for a phase lag of several degrees in the measurement electronics.) For quasi-static PFM measurements [16], the response of the N-polar domains is predicted to be in-phase with the applied voltage ($\varphi_{drv} = 0^\circ$), i.e. the piezoelectric strain is tensile (or compressive) when the tip bias is positive (or negative)



relative to the N-polar surface, while the response of the Al-polar domains is predicted to be out-of-phase ($\varphi_{drv} = 180^\circ$). However, a phase retardation of approximately 90° (relative to quasi-static conditions) occurs at the first CR frequency (f_1^c). Hence, the low-phase ($\varphi_{drv} \approx -95^\circ$) regions in the electrically driven phase image are ascribed to N-polar domains, and the high-phase ($\varphi_{drv} \approx +86^\circ$) in the electrically driven phase image are ascribed to Al-polar domains. By comparing the electrically driven amplitude image (figure 3(a)) and Q image (figure 3(b)) with the electrically driven phase image (figure 3(c)), it is seen that the amplitude and Q vary in a manner correlated with piezoelectric polarity. The electrically driven amplitude is slightly lower, on average, in Al-polar domains than N-polar domains, and the electrically driven Q is substantially higher in Al-polar domains than N-polar domains.

Comparison of the mechanically driven amplitude, Q, and phase images (second row) with the corresponding electrically driven images (first row) enables distinguishing electromechanical or electrostatic phenomena from purely mechanical phenomena. The variation within the image area of the mechanically driven amplitude, Q, and phase is seen to be much smaller than the variation of the corresponding electrically driven parameters. Further, the mechanically driven parameters do not show domain contrast (i.e. variation correlated with piezoelectric polarity).

The probability plots in figure 3(h) show the distributions of electrically driven amplitude in N-polar domains (red curve), electrically driven amplitude in Al-polar domains (green curve), mechanically driven amplitude in N-polar domains (blue curve), and mechanically driven amplitude in Al-polar domains (magenta curve). The probability plots in figures 3(i) and (j) show the analogous distributions for Q and phase. To create the probability plots, a masking procedure was devised that classifies individual pixels as belonging to N-polar or Al-polar domains. A pixel was assigned to the 'N-polar mask' if the electrically driven phase (figure 3(c)) lies within a specific range around $\varphi_{drv} = -95^\circ$, or was assigned to the 'Al-polar mask' if the electrically driven phase lies within a specific range around $\varphi_{drv} = +86^\circ$. The N-polar and



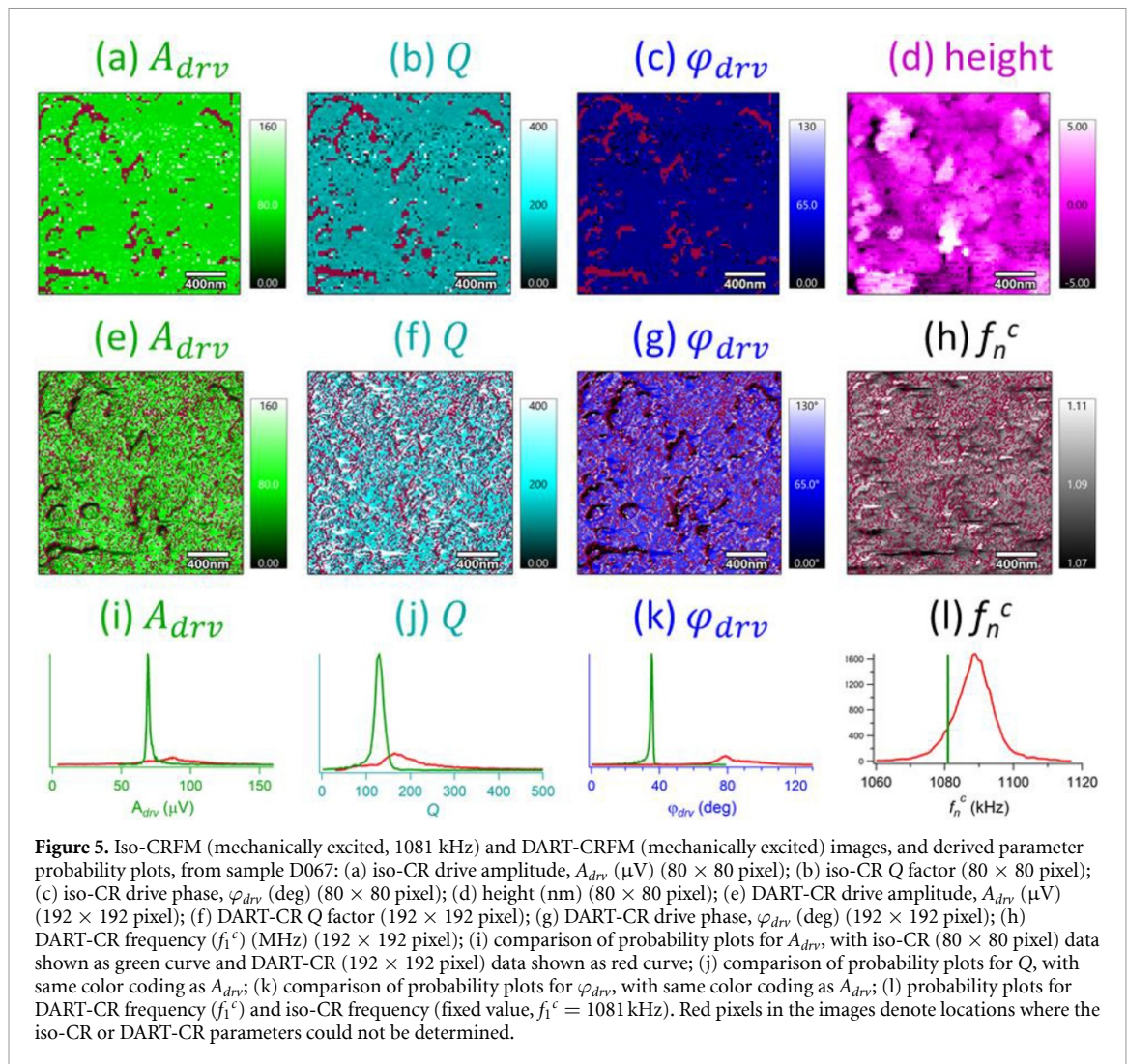
Al-polar masks created with this procedure were then used to calculate probability plots that show the amplitude, Q, and phase distributions within the Al-polar and N-polar domains. The probability plots confirm the conclusions drawn from inspection of the images: the electrically driven amplitude is slightly lower in Al-polar than N-polar domains, the electrically driven Q is substantially higher in Al-polar domains, and the mechanically driven amplitude, Q, and phase do not show domain contrast.

The height image, figure 3(d), and corresponding frequency vs. domain type plots, figure 3(k), show that the average height of the N-polar domains is ≈ 0.8 nm larger than the average height of the Al-polar domains; further, sample locations at the high end of the height distribution belong almost entirely to N-polar domains. These results suggest that the piezoelectric polarity affects the AlN growth rate.

Iso-CR amplitude, Q, and phase imaging results for samples D068 (Al-polar) and D069 (N-polar) are shown in the supplementary data, figures S1 and S2. Crossing force ($F_{t,cr}$) and adhesion force (F_{adh}) imaging results for sample D067 are shown in the supplementary data, figure S3. Possible mechanisms for the polarity dependence of the CR amplitude and Q are discussed below in section 5.

4.3. Comparison of iso-CR and DART-CR imaging

Electrically excited iso-CR and DART-CR images and probability plots from a selected area of sample D067 (different than the area examined in figure 3) are compared in figure 4, and the corresponding mechanically



excited images and probability plots are compared in figure 5. The displayed parameters are drive amplitude (A_{drv}) (first column), Q factor (Q) (second column), drive phase (φ_{drv}) (third column), surface height (fourth column), and DART frequency (f_1^c) (also fourth column). (For comparison with the DART results, note that all the iso-CR images in figures 4 and 5 were acquired at a fixed frequency of 1.081 MHz.) The parameters are color-coded as follows: green for A_{drv} , cyan (blue-green) for Q , blue for φ_{drv} , magenta for height, and gray for f_1^c . The first rows of figures 4 and 5 show iso-CR images with 80×80 resolution; the second row of figure 4 shows iso-CR images with 200×200 resolution; the third row of figure 4 and the second row of figure 5 show DART images with 192×192 resolution; the fourth row of figure 4 and the third row of figure 5 show probability plots that summarize the imaging results. (Note that each probability plot in figures 4(m)–(o) and 5(i)–(k) is normalized to the number of the pixels in the corresponding image. Before normalization, the peak heights for the iso-CR-PFM (200×200 pixel) probability plots (blue curves in figures 4(m)–(o)) were much greater than the peak heights for the iso-CR-PFM (80×80 pixel) probability plots (green curves). With normalization, the peak heights for the iso-CR-PFM (200×200 pixel) and iso-CR-PFM (80×80 pixel) plots are similar.)

The main conclusion from comparison of the iso-CR and DART-CR images and probability plots is that the pixel-scale variation of f_1^c in DART (figures 4(i), (p) and in 5(h), (l)) leads to a pixel-scale variation of the CR fit parameters (A_{drv} , Q , and φ_{drv}), which causes a broadening of the DART-CR parameter distributions (red curves in figures 4(m)–(o) and in 5(i)–(k)) as compared to the iso-CR parameter distributions (green and blue curves). This is direct experimental confirmation of the primary advantage of iso-CR over DART-CR. By eliminating the pixel-scale variation of f_1^c , the iso-CR method removes any f_1^c -dependent variation of the CR fit parameters, thus enabling more direct observation of the parameter variation (image contrast) that arises from spatially varying material properties within the sample.

Comparison of the probability plots associated with the iso-CR-PFM (80×80 pixel) images (green curves in figures 4(m)–(o)) and the probability plots associated with the iso-CR-PFM (200×200 pixel)

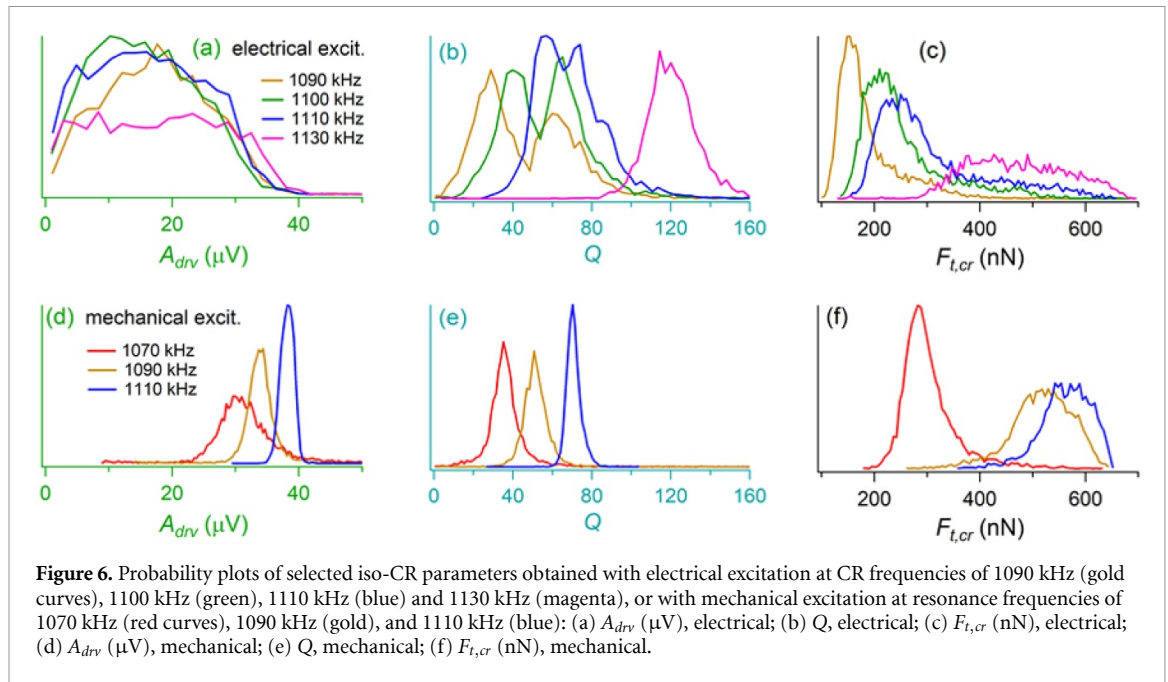


Figure 6. Probability plots of selected iso-CR parameters obtained with electrical excitation at CR frequencies of 1090 kHz (gold curves), 1100 kHz (green), 1110 kHz (blue) and 1130 kHz (magenta), or with mechanical excitation at resonance frequencies of 1070 kHz (red curves), 1090 kHz (gold), and 1110 kHz (blue): (a) A_{drv} (μV), electrical; (b) Q , electrical; (c) $F_{t,cr}$ (nN), electrical; (d) A_{drv} (μV), mechanical; (e) Q , mechanical; (f) $F_{t,cr}$ (nN), mechanical.

images (blue curves in figures 4(m)–(o)) shows that going from lower (80×80 pixel) to higher (200×200 pixel) resolution has very little effect on the fit parameter distributions, as expected.

A_{drv} , with iso-CR (80×80 pixel) data shown as green curve, iso-CR (200×200 pixel) data shown as blue curve, and DART-CR (192×192 pixel) data shown as red curves; (n) probability plots for Q , with same color coding as A_{drv} ; (o) probability plots for φ_{drv} , with same color coding as A_{drv} ; (p) probability plots for DART-CR frequency (f_1^c) and iso-CR frequency (fixed value, $f_1^c = 1081$ kHz). Red pixels in the images denote locations where the iso-CR or DART-CR parameters could not be determined.

4.4. Frequency dependence of iso-CR parameters

Probability plots of A_{drv} , Q , and $F_{t,cr}$, measured with electrical or mechanical excitation, for several values of f_1^c , are shown in figure 6. To facilitate visual comparison of the results, for each parameter the x -axis range for electrical excitation (figures 6(a)–(c)) matches the x -axis range for mechanical excitation (figures 6(d)–(f)).

The A_{drv} and Q are seen to increase with increasing f_1^c for mechanical excitation (figures 6(d) and (e)). The peak amplitude, which is the product of A_{drv} and Q , thus shows an even larger relative increase with f_1^c . The width of the mechanically excited A_{drv} distribution narrows with increasing f_1^c . This narrowing might be due to the correlation between increasing f_1^c and increasing contact force (F_c). For a fixed-amplitude AC mechanical (photothermal) excitation, the ratio of the AC component to the DC component of the total contact force will decrease with increasing DC contact force, hence any non-linearity in the response of the tip-sample system to the AC mechanical excitation will decrease with increasing DC contact force.

For electrical excitation, the width of the amplitude distribution (figure 6(a)) broadens slightly with increasing f_1^c . The width of the Q distribution (figure 6(b)) narrows with increasing f_1^c , and in addition the Q distribution changes from a bimodal (double-peaked) shape at low f_1^c to a unimodal shape at high f_1^c .

To provide more insight into the frequency dependencies of the A_{drv} and Q distributions, imaging results for electrical and mechanical excitation are shown in figures 7 and 8 respectively. The φ_{drv} image for electrical excitation at 1110 kHz is shown in figure 7(i) (repeated from figure 3(c)) to identify the N-polar and Al-polar domains. For electrical excitation at the lowest frequency, the A_{drv} is lower (figure 7(a)) and Q is higher (figure 7(e)) in Al-polar than N-polar domains. (The domain contrast is more distinct in the Q image than the A_{drv} image.) The contrast between the Al-polar and N-polar domains decreases with increasing f_1^c , for the electrically excited A_{drv} and Q images. In addition, the average Q increases with increasing f_1^c , while the average A_{drv} shows little change with f_1^c . There is no visible contrast between Al-polar and N-polar domains in the electrically excited Q image obtained at the highest frequency (figure 7(h)). In the mechanically excited A_{drv} and Q images (figure 8), the average parameter value (A_{drv} or Q) increases with increasing f_1^c , and the image contrast decreases with increasing f_1^c . The contrast within the mechanically excited A_{drv} and Q images at $f_1^c = 1070$ kHz (figures 8(a) and (d)) does not show an obvious correlation with the piezoelectric domain structure (figure 7(i)).

The φ_{drv} image for electrical excitation at 1110 kHz is shown in figure 7(i) (repeated from figure 3(c)) to identify the N-polar and Al-polar domains. For electrical excitation at the lowest frequency, the A_{drv} is lower

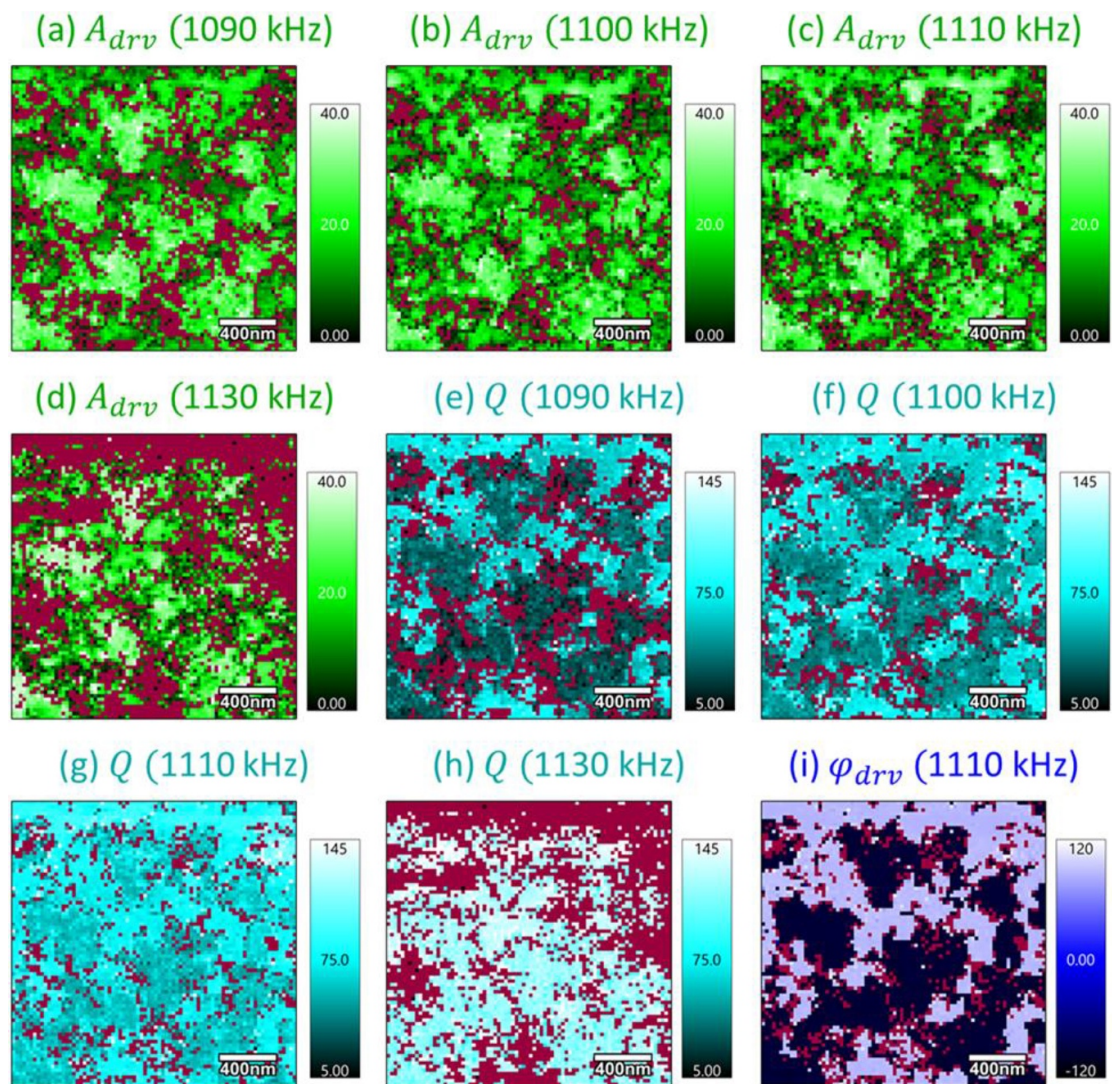


Figure 7. Images of iso-CR-PFM A_{drv} , Q , and φ_{drv} obtained with electrical excitation at various CR frequencies: (a) A_{drv} (μV), 1090 kHz; (b) A_{drv} (μV), 1100 kHz; (c) A_{drv} (μV), 1110 kHz; (d) A_{drv} (μV), 1130 kHz; (e) Q , 1090 kHz; (f) Q , 1100 kHz; (g) Q , 1110 kHz; (h) Q , 1130 kHz; (i) φ_{drv} (deg), 1110 kHz.

(figure 7(a)) and Q is higher (figure 7(e)) in Al-polar than N-polar domains. (The domain contrast is more distinct in the Q image than the A_{drv} image.) The contrast between the Al-polar and N-polar domains decreases with increasing f_1^c , for the electrically excited A_{drv} and Q images. In addition, the average Q increases with increasing f_1^c , while the average A_{drv} shows little change with f_1^c . There is no visible contrast between Al-polar and N-polar domains in the electrically excited Q image obtained at the highest frequency (figure 7(h)). In the mechanically excited A_{drv} and Q images (figure 8), the average parameter value (A_{drv} or Q) increases with increasing f_1^c , and the image contrast decreases with increasing f_1^c . The contrast within the mechanically excited A_{drv} and Q images at $f_1^c = 1070$ kHz (figures 8(a) and (d)) does not show an obvious correlation with the piezoelectric domain structure (figure 7(i)).

Probability plots comparing the A_{drv} , Q and φ_{drv} distributions within the Al-polar and N-polar domains, with electrical excitation at different values of, re shown in figure 9. These probability plots were obtained by the same domain masking procedure (described in section 4.2) as the probability plots in figure 3. The results of figure 9 confirm that the A_{drv} and Q within the two domain types differ at low f_1^c , and the domain contrast diminishes with increasing f_1^c . In addition, the widths of the φ_{drv} distributions decrease, and the separation between the peaks of the phase distributions for the two domain types approaches 180° , with increasing f_1^c .

Median A_{drv} and Q values calculated for electrical excitation in N-polar domains (red triangles), electrical excitation in Al-polar domains (green inverted triangles), mechanical excitation in N-polar domains (blue squares), and mechanical excitation in Al-polar domains (magenta circles) are plotted as functions of f_1^c in figures 10(a) and (b) respectively. These plots show that the median A_{drv} and Q values for electrical excitation are polarity dependent, while the corresponding values for mechanical excitation are not polarity dependent. The relative difference between the median A_{drv} (or Q) value in N-polar domains and the median A_{drv} (or Q)

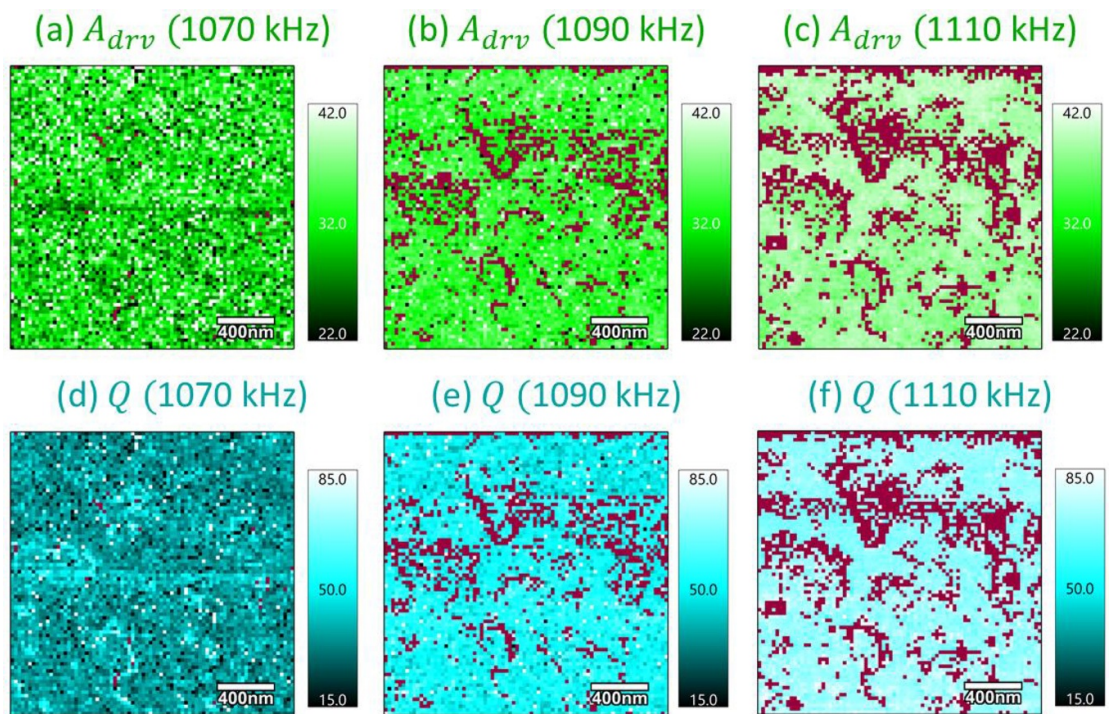


Figure 8. Images of iso-CR A_{drv} and Q obtained with mechanical excitation at various CR frequencies: (a) A_{drv} (μV), 1070 kHz; (b) A_{drv} (μV), 1090 kHz; (c) A_{drv} (μV), 1110 kHz; (d) Q , 1070 kHz; (e) Q , 1090 kHz; (f) Q , 1110 kHz.

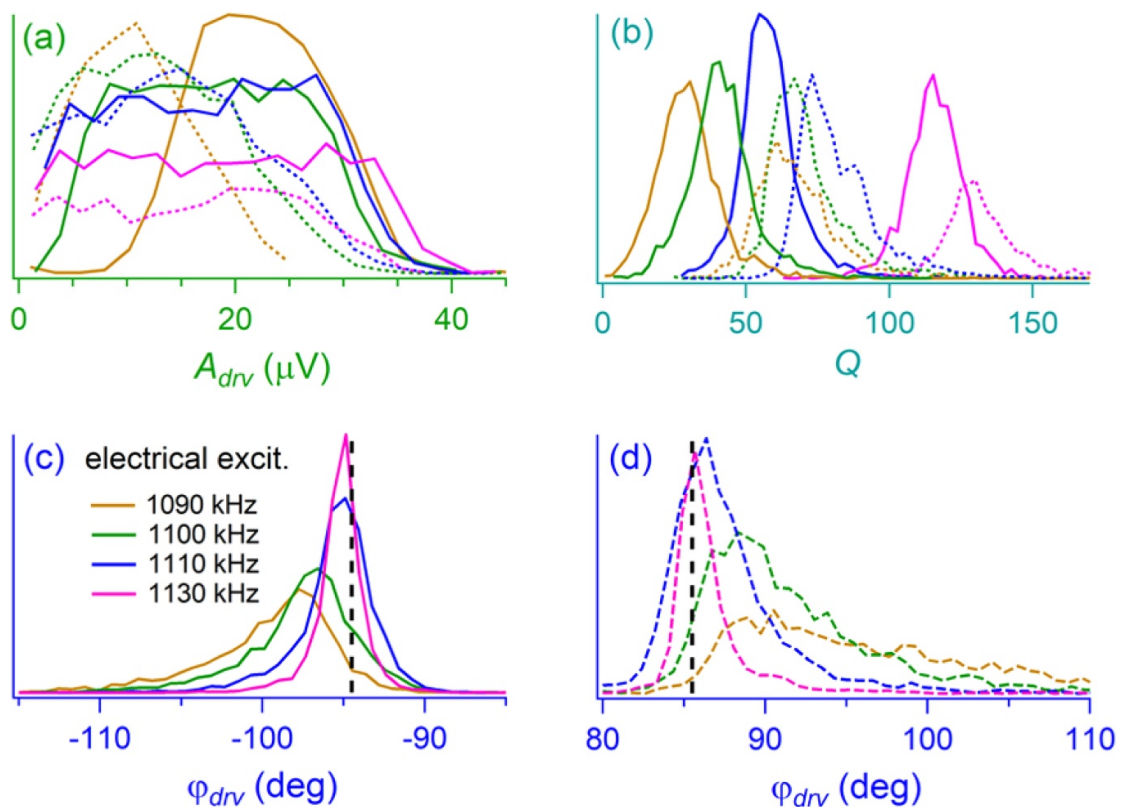
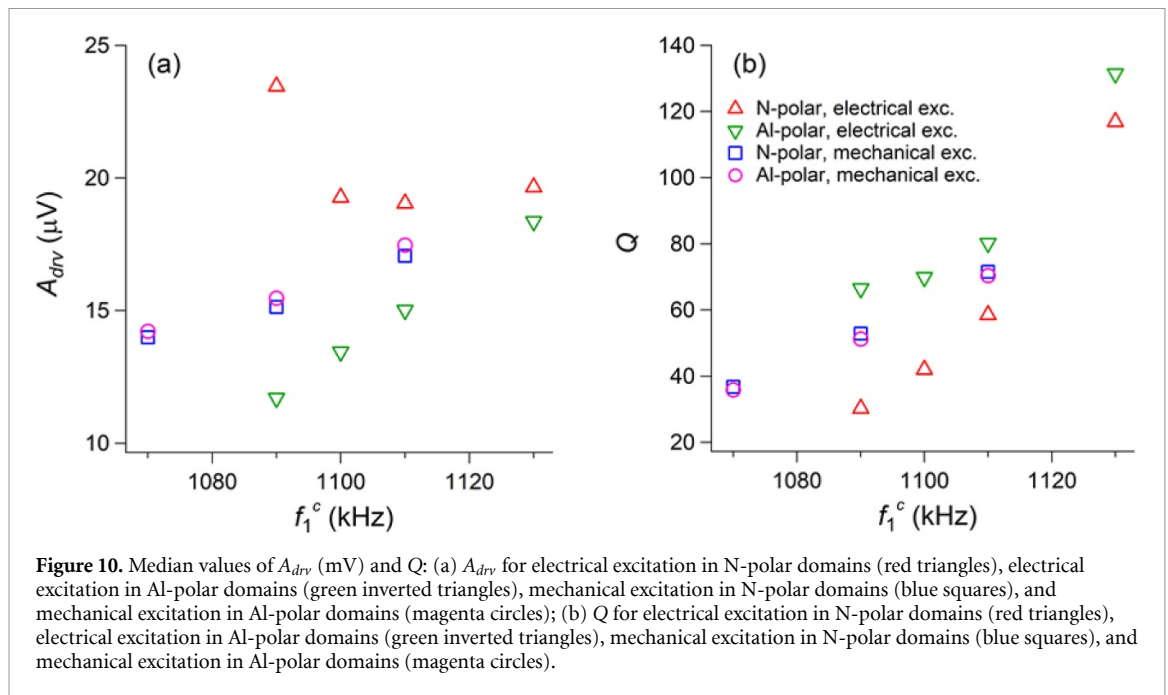


Figure 9. Probability plots of iso-CR-PFM parameters measured within N-polar (solid lines) and Al-polar (dashed lines) domains, for electrical excitation at CR frequencies of 1090 kHz (gold), 1100 kHz (green), 1110 kHz (blue), and 1130 kHz (magenta). (a) A_{drv} (μV); (b) Q ; (c) φ_{drv} (deg), N-polar domains (vertical dashed line indicates φ_{drv} of -94.5°); (d) φ_{drv} (deg), Al-polar domains (vertical dashed line indicates φ_{drv} of -85.5°).



value in Al-polar domains is seen to decrease with increasing f_1^c (i.e. the polarity dependence of these parameters decreases with increasing f_1^c).

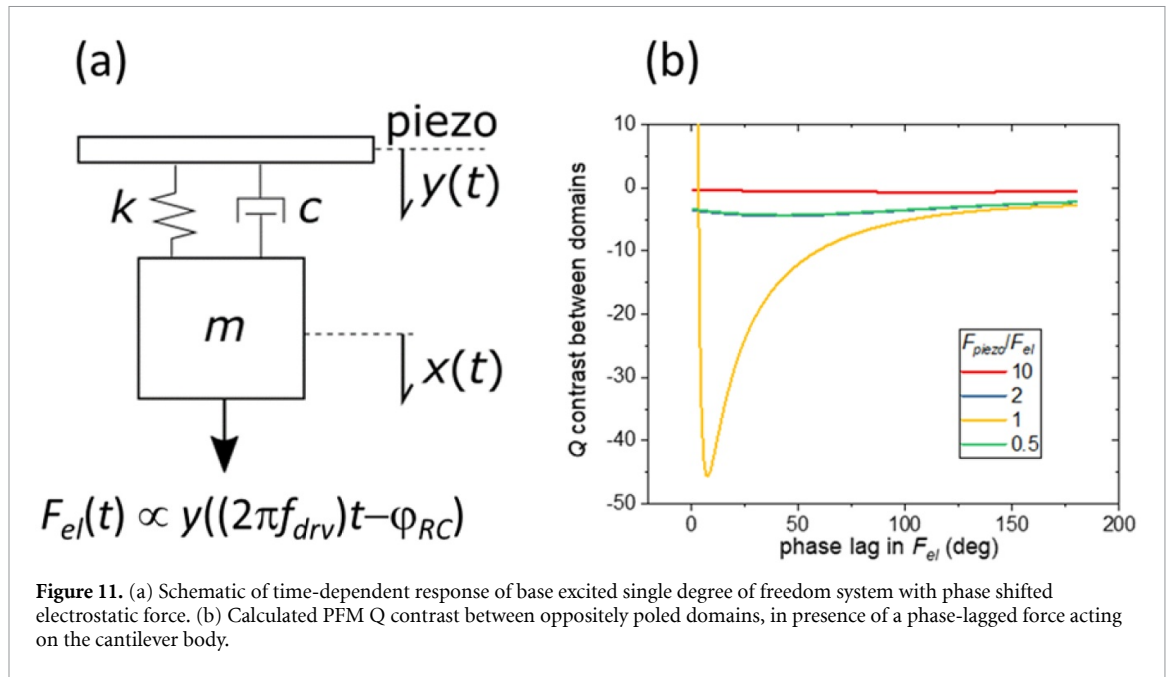
A warning must be made about comparison of the electrically excited and mechanically excited A_{drv} values in figure 10(a). Because of the difference in drive mechanism, quantitative comparison of electrically and mechanically (photothermally) excited amplitudes is not possible. The mechanically excited A_{drv} values displayed in figure 10(a) were multiplied by an arbitrary factor (0.45) to make the mechanically excited values to appear to lie between the electrically excited values in N-polar domains and the electrically excited values in Al-polar domains. On the other hand, because Q is a dimensionless parameter, the comparison of the electrically and mechanically excited Q values in figure 10(b) is valid. (Thus, Q is more useful than A_{drv} for comparing CR measurement results across multiple excitation schemes.)

5. Discussion

By precisely controlling f_1^c in the iso-CR method for both electrical (figures 6(a)–(c), 7 and 9) and mechanical (figures 6(d)–(f) and 8) excitation, we gain specific insight into the origin of the image contrast. The N-polar domains and Al-polar domains have the same crystal structure and were grown under the same conditions, differing only in polarity. It thus seems unlikely that the N-polar and Al-polar domains have intrinsically different mechanical or electromechanical properties. Mechanically excited iso-CR reveals the expected findings; N-polar and Al-polar domains exhibit similar Q distributions, confirming that no dissipative contrast (i.e. internal friction or loss tangent) exists between domains. When varying f_1^c , the relative Q contrast is maintained, but the absolute value of Q increases with increasing f_1^c , as expected for the modal damping contribution for this cantilever.

Before examining the results in more detail, consider the ideal case in which ‘pure’ CR-PFM measurements (with no electrostatic artifacts or other complicating factors) are made on a piezoelectric sample consisting of domains with ‘up’ or ‘down’ polarity. In this case, the drive amplitude and Q would be the same over ‘up’ and ‘down’ domains, and the drive phase would shift by 180° when traversing a domain boundary.

The polarity dependence of the drive amplitude and Q in electrically excited iso-CR-PFM, and the difference in Q between electrically and mechanically excited iso-CRPFM, is attributed to an electrostatic artifact contribution to the experimetal PFM response. This assertion is bolstered by considering the deviation of the drive phase difference between Al-polar and N-polar domains from the ideal 180° phase shift. Electrostatic artifacts have been found to contribute to the apparent PFM response (i.e. the total cantilever deflection at the frequency of the AC tip-sample voltage) in piezoelectric, ferroelectric, and non-piezoelectric materials [23–25]. Electrostatic artifacts arise because the near-surface AC electric fields in the sample (induced by the tip-sample voltage) modulate the near-surface electronic charge density or dipole density.



This modulation in turn produces an AC component of the sample electrostatic force on the cantilever (at the drive frequency), which is given by the following general expression [26]:

$$F_{el} = \frac{\partial C_{TS}}{\partial z} (V_{cp} + V_{dc}) V_{ac} \sin(2\pi f_{drv}(t - R_{TS}C_{TS})) , \quad (13)$$

where $\frac{\partial C_{TS}}{\partial z}$ is the gradient of the tip-sample capacitance in the vertical (z) direction, V_{cp} is the built-in contact potential difference between the tip and sample, V_{dc} is the applied DC bias, V_{ac} is the amplitude of the applied AC bias, f_{drv} is the drive frequency, R_{TS} is the series resistance of the tip-sample circuit, and t is time. Note that F_{el} is phase-delayed by an amount $\varphi_{RC} = 2\pi f_{drv} R_{TS} C_{TS}$ relative to the AC bias due to the RC time constant of the tip-sample circuit. In our experiments $V_{dc} = 0$, hence non-zero V_{cp} is needed to produce an observable F_{el} .

Because the tip is in contact with the sample in PFM, the total electrostatic force can be divided into a short-range force acting on the tip, called the tip electrostatic (TES) force, and a distributed long-range force acting on the entire body of the cantilever, called the body electrostatic (BES) force [25]. The TES force may produce short-range image contrast, on the same length scale as true PFM; the BES force will produce a ‘background’ signal that is uniform or slowly varying over the image area because of the large ratio of the cantilever length (125 μm) to the image size (2 μm).

Recent experimental and modeling studies examined the frequency dependence of the measured cantilever response in PFM [25] and ESM [27]. The focus of the PFM study was on comparing the responses for the first and higher flexural eigenmodes; however, figures 5(a) and (b) from the PFM study [25] show that the ratio of the electrostatic to PFM contributions to the deflection signal decreases when the static tip-sample contact stiffness k_{TS} increases for a given eigenmode. This reduced electrostatic contribution is less pronounced than for increasing eigenmode number, but similarly originates from an increased dynamic stiffness of the cantilever. Figure 11 from the ESM study [27] shows that the TES (or ‘local electrostatic’) and BES (or ‘non-local electrostatic’) contributions to the deflection amplitude decrease with increasing frequency, while the surface displacement induced amplitude increases with increasing frequency. In comparing the present work to these results, it should be pointed out that the static cantilever stiffness was significantly higher here (24.4 N m^{-1}) than in the PFM study where several cantilevers were used with static stiffnesses of $\approx 2 \text{ N m}^{-1}$, $\approx 0.2 \text{ N m}^{-1}$, and $\approx 0.006 \text{ N m}^{-1}$, or the ESM study where the static stiffness was $\approx 1 \text{ N m}^{-1}$. Using a cantilever of relatively high static stiffness, and going to high tip-sample contact force (up to 610 nN), facilitates attaining a small ratio of electrostatic to PFM deflections for the first flexural eigenmode.

5.1. Iso-CR-PFM phase contrast

The true PFM (surface displacement) response is 180° out of phase for ‘up’ and ‘down’ domains for ideal oppositely poled domains. On the other hand, the phase of the TES response (due to modulation of the

surface charge or surface dipole density) is likely to show little change when the tip moves from an ‘up’ to ‘down’ domain, and the phase of the BES response is necessarily uniform because of the long range of the BES force. If the phase of the total electrostatic response is uniform, or nearly uniform, over the image area, then the electrostatic response will add to the PFM response and increase the total deflection for domains of one polarity, but will subtract from the PFM response and reduce the total deflection for domains of the other polarity, resulting in amplitude contrast between domains. The dependence of the drive phase contrast on CR frequency provides further evidence for the presence of electrostatic artifacts. As f_1^c increases, the drive phase difference between domains increases and moves closer to 180° , as shown in figures 9(c) and (d).

5.2. Iso-CR-PFM amplitude contrast

The probability plots in figure 9(a) show that the distribution of drive amplitudes within each type of domain is very broad at the higher resonance frequencies. There are significant contributions to the amplitude probability plots at 1110 kHz and 1130 kHz from amplitudes near zero. A basic understanding of the PFM mechanism implies that regions of near-zero amplitude should occur around the boundaries between the ‘up’ and ‘down’ domains in a sample containing ‘up’ (e.g. Al-polar AlN) and ‘down’ (e.g. N-polar AlN) domains. Indeed, zero signal at boundaries between ‘up’ and ‘down’ domains is considered to be a test of the accuracy of PFM measurements. The measured PFM amplitude near a domain boundary is expected to shift away from zero when an electrostatic artifact is present. This may explain why near-zero amplitudes are less prevalent in the amplitude probability plots at the lower CR frequencies (where the ratio of electrostatic to piezoelectric response is larger).

The probability plots (figure 9(a)) show that higher amplitudes are measured in N-polar than Al-polar domains, even at the highest CR frequency (compare the solid and dashed magenta curves). The median value plot (figure 10(a)) shows that the median amplitude is lower in Al-polar than N-polar domains, even at the highest CR frequency. As already suggested, the amplitude contrast between domains may arise from different combinations of electrostatic and piezoelectric forces over the two domain types. However, another amplitude contrast mechanism is possible: the Al-polar domains are known to originate from polarity reversal during growth, such that each Al-polar domain lies on top of an N-polar layer rather extending all the way to the AlN-Si(substrate) interface. Thus, if the AC electric field in the sample (induced by the AC tip bias) penetrates through an Al-polar domain into the underlying N-polar domain, the compressive (or tensile) strain in the Al-polar domain will be partially cancelled by tensile (or compressive) strain in the underlying N-polar domain, causing an overall reduction in the CR-PFM amplitude. This mechanism would naturally lead to lower amplitude over Al-polar domains, which is consistent with the results. The electrostatic and strain-cancellation mechanisms for the amplitude contrast are both plausible, and we do not have sufficient quantitative knowledge of the electromechanical and electrostatic interactions to determine which mechanism is dominant (e.g. the average depth below the surface for the polarity domain reversal, and the penetration depth of the AC electric field, are unknown).

5.3. Iso-CR-PFM Q contrast

The images of figures 7(e)–(h) and probability plots of figure 9(b) show the electrically driven Q values depend strongly on polarity, especially at lower f_1^c where the ratio of electrostatic to piezoelectric response is largest. The mechanically driven Q values (figure 6(e)) differ from the electrically driven values (figure 6(b)) and do not depend on polarity (figures 8(d)–(f)). The polarity dependence of the electrically driven Q, and shifts between the electrically and mechanically driven Q, cannot be explained within the standard beam models previously used to describe CRFM. In a typical homogeneous solution to such a beam model [3], the CR Q factor depends only on f_1^c and damping within the sample. Prior analyses with an external driving force [2] determined that the location of the drive force (e.g. at the tip or the cantilever base) does not influence Q. In a spatial solution to the beam model, the combination of electrostatic and surface-displacement drive forces modifies the amplitude of the resonance peak, but does not affect Q.

Here we propose a simple point-mass model that can explain, at least qualitatively, the experimental Q contrast. The key feature of the new model is a ‘secondary’ AC force on the cantilever that is both phase-shifted and spatially separated from the ‘primary’ force. In our experiments, the primary force is the surface displacement (piezoelectric) force and the secondary force is the BES force. As discussed above (see equation (13)), the electrostatic force is expected to be phase lagged relative to the tip bias by $\varphi_{RC} = 2\pi f_{drv} R_{TS} C_{TS}$, while the surface displacement force is in phase with the tip bias over N-polar domains, and 180° out of phase over Al-polar domains. (In MacDonald *et al* [25], the authors also proposed that a phase lag between surface-displacement and electrostatic forcing must exist.) Further, the surface displacement force acts on the tip, while the BES force is distributed along the cantilever, providing the required spatial separation. Figure 11(a) depicts a DHO model where drive forces, representing the surface

displacement force and phase-lagged electrostatics force, act on either side of the spring-dashpot system. The frequency-dependent response of the modeled system to the drive forces is given by

$$\frac{x(f_{drv})}{y(f_{drv})} = \frac{1 + \frac{if_{drv}}{f_1^c Q} + \frac{B}{m(2\pi f_1^c)^2} e^{-i\varphi_{RC}}}{1 - \left(\frac{f_{drv}}{f_1^c}\right)^2 + i\left(\frac{f_{drv}}{f_1^c Q}\right)}, \quad (14)$$

where $x(f_{drv})$ is the steady-state displacement of the point-mass oscillator (i.e. the AFM cantilever) in frequency space, $y(f_{drv})$ is the steady-state base excitation input (i.e. the PFM surface displacement), $F_{el}(t)$ is a phase-lagged electrostatic force that is proportional to the base excitation input and phase shifted by an amount φ_{RC} , f_1^c is the natural frequency of the single degree of freedom system (i.e. the first CR frequency), m is the equivalent mass of the system, k is the equivalent stiffness, c is the equivalent damping, B is a parameter that modulates the magnitude of the external forcing to the system, and t (in figure 11(a)) is time.

Figure 11(b) shows calculations for a change in Q between two 180° offset base excitations (which represent the surface displacement forces over N-polar or Al-polar domains) in the presence of another drive force of varying phase lag (which represents the BES force). Results are shown for multiple values of the ratio of surface-displacement drive force F_{piezo} to electrostatic drive force F_{el} . In the absence of the electrostatic force, the model is set to $Q = 100$. When the two drive forces are of similar magnitude, the measured Q can be increased by 50% or decreased by 20%. The effect is reduced as either drive force becomes more dominant in magnitude, but the effect remains $\approx 5\%$ even if the electrostatic force is half the magnitude of the surface-displacement force. The finding indicates that unexpected Q contrast can be a sensitive indicator of the presence of ‘secondary’ drive forces that are phase and location shifted relative to the ‘primary’ force, and that the possibility of such secondary drive forces should be considered anytime absolute Q measurements are made (e.g. for viscoelastic measurements).

A previous experimental study [28] supports our model for the origin of the Q contrast. In that study, the tip was held $1 \mu\text{m}$ above the sample in an ultra-high-vacuum environment. A conventional shaker piezo drive produced an AC force on the base of the cantilever. An AC voltage, proportional to but phase-lagged by 90° relative to the deflection signal, was applied to the tip, creating a phase-lagged BES force on the cantilever. A DC voltage on the sample provided another control element. Giant changes in Q were induced by controlling the AC and DC voltages, with Q varying from 400 to 104 000 for a particular cantilever.

To summarize, the frequency (f_1^c) dependence of the drive phase, drive amplitude, and Q contrast between domains suggests a convergence to a pure PFM response (180° out of phase, with equal amplitude and Q) at high f_1^c . However, measurable drive amplitude and Q contrast persists at the highest examined f_1^c , with lower drive amplitude and higher Q over the Al-polar domains. As discussed, the lower drive amplitude over the Al-polar domains may arise from an electrostatic contribution, or from partial strain cancellation due to field penetration into an underlying N-polar layer. On the other hand, according to our model, the Q contrast can arise only from a BES contribution (because the BES force is phase-lagged and spatially separated from the surface displacement force). In the present state of development of the model, it is not possible to quantify and subtract the electrostatic artifact contributions from the experimental values of drive amplitude and Q .

6. Conclusion

We implement a new contact resonance AFM imaging technique, isomorphic contact resonance (iso-CR), which utilizes the force-volume mapping mode of the AFM to attain a constant CR frequency, and hence constant tip-sample contact stiffness and invariant vibrational shape of the cantilever, for all pixels in the image. The iso-CR technique is demonstrated by acquiring iso-CR-PFM (with electrical excitation of the tip-sample contact) and iso-CR-FM (with photothermal excitation of the cantilever) images of a piezoelectric AlN thin film, grown epitaxially on Si, that contains nanoscale Al-polar (or ‘up’) and N-polar (or ‘down’) domains. Images are acquired at several resonance frequencies for the first flexural CR mode. The CR fit parameters, including drive amplitude, drive phase, and Q , show contrast between Al-polar and N-polar domains in the iso-CR-PFM images, but the domain contrast does not occur in the corresponding iso-CR-FM images. The PFM drive amplitude is lower in Al-polar than N-polar domains, and the PFM Q is higher in Al-polar than N-polar domains, at low CR frequency. The domain contrast of the PFM drive amplitude and Q decreases strongly with increasing frequency. Finally, the PFM drive phase contrast between domains increases and approaches 180° with increasing frequency. These frequency dependent domain contrast effects in iso-CR-PFM are ascribed primarily to electrostatic contributions to the cantilever deflection. The electrostatic contributions decrease with increasing CR frequency, so that the signal is mostly piezoelectric at the highest frequency. To conclude, the demonstration experiments presented in this work illustrate the

promise of iso-CR for quantitative mapping and frequency dependence analysis of the entire range of material properties that have heretofore been investigated by CRFM methods, such as indentation modulus, viscoelastic loss tangent, and piezoelectric coefficient.

ORCID iDs

Lawrence H Robins  <https://orcid.org/0000-0002-1063-7115>

Matt D Brubaker  <https://orcid.org/0000-0002-3818-4939>

Ryan C Tung  <https://orcid.org/0000-0003-2862-6980>

Jason P Killgore  <https://orcid.org/0000-0002-8458-6680>

References

- [1] Hurley D C 2009 Contact resonance force microscopy techniques for nanomechanical measurements *Applied Scanning Probe Methods XI. NanoScience and Technology*, ed B Bhushan and H Fuchs (Berlin: Springer-Verlag) ch 5 pp 97–138
- [2] Rabe U 2006 Atomic force acoustic microscopy *Applied Scanning Probe Methods II. NanoScience and Technology*, ed B Bhushan and H Fuchs (Berlin: Springer-Verlag) ch 2 pp 37–90
- [3] Yuya P A, Hurley D C and Turner J A 2008 Contact-resonance atomic force microscopy for viscoelasticity *J. Appl. Phys.* **104** 074916
- [4] Killgore J P and DelRio F W 2018 Contact resonance force microscopy for viscoelastic property measurements: from fundamentals to state-of-the-art applications *Macromolecules* **51** 6977–96
- [5] Okino H, Sakamoto J and Yamoto T 2003 Contact-resonance piezoresponse force microscope and its application to domain observation of $\text{Pb}(\text{Mg}(1/3)\text{Nb}(2/3))\text{O}_3\text{-PbTiO}_3$ single crystals *Jpn. J. Appl. Phys.* **42** 6209–13
- [6] Balke N, Jesse S, Morozovska A N, Eliseev E, Chung D W, Kim Y, Adamczyk L, Garcia R E, Dudney N and Kalinin S V 2010 Nanoscale mapping of ion diffusion in a lithium-ion battery cathode *Nat. Nanotechnol.* **5** 749–54
- [7] Balke N, Jesse S, Kim Y, Adamczyk L, Tselev A, Ivanov I N, Dudney N J and Kalinin S V 2010 Real space mapping of Li-ion transport in amorphous Si anodes with nanometer resolution *Nano Lett.* **10** 3420–5
- [8] Gannepalli A, Yablon D G, Tsou A H and Proksch R 2011 Mapping nanoscale elasticity and dissipation using dual frequency contact resonance AFM *Nanotechnology* **22** 355705
- [9] Jesse S, Kalinin S V, Proksch R, Baddorf A P and Rodriguez B J 2007 The band excitation method in scanning probe microscopy for rapid mapping of energy dissipation on the nanoscale *Nanotechnology* **18** 435503
- [10] Kos A B and Hurley D C 2008 Nanomechanical mapping with resonance tracking scanned probe microscope *Meas. Sci. Technol.* **19** 015504
- [11] Kos A B, Killgore J P and Hurley D C 2014 SPRITE: a modern approach to scanning probe contact resonance imaging *Meas. Sci. Technol.* **25** 025405
- [12] Balke N, Jesse S, Yu P, Carmichael B, Kalinin S V and Tselev A 2016 Quantification of surface displacements and electromechanical phenomena via dynamic atomic force microscopy *Nanotechnology* **27** 425707
- [13] Killgore J P, Deolia A, Robins L H and Murray T 2019 Experimental reconstruction of the contact resonance shape factor for quantification and amplification of bias-induced strain in atomic force microscopy *Appl. Phys. Lett.* **114** 133108
- [14] Wagner R, Raman A and Proksch R 2013 Spatial spectrograms of vibrating atomic force microscopy cantilevers coupled to sample surfaces *Appl. Phys. Lett.* **103** 263102
- [15] Wagner R, Killgore J P, Tung R C, Raman A and Hurley D C 2015 Vibrational shape tracking of atomic force microscopy cantilevers for improved sensitivity and accuracy of nanomechanical measurements *Nanotechnology* **26** 045701
- [16] Brubaker M D, Duff S M, Harvey T E, Blanchard P T, Roshko A, Sanders A W, Sanford N A and Bertness K A 2016 Polarity-controlled GaN/AlN nucleation layers for selective-area growth of GaN nanowire arrays on Si(111) substrates by molecular beam epitaxy *Cryst. Growth Des.* **16** 596–604
- [17] Roshko A, Brubaker M D, Blanchard P T, Harvey T E and Bertness K A 2019 The role of Si in GaN/AlN/Si(111) plasma assisted molecular beam epitaxy: polarity and inversion *Jpn. J. Appl. Phys.* **58** SC1050
- [18] Sader J E, Chon J W M and Mulvaney P 1999 Calibration of rectangular atomic force microscope cantilevers *Rev. Sci. Instrum.* **70** 3967–9
- [19] Sader J E, Sanelli J A, Adamson B D, Monty J P, Wei X, Crawford S A, Friend J R, Marusic I, Mulvaney P and Bieske E J 2012 Spring constant calibration of atomic force microscope cantilevers of arbitrary shape *Rev. Sci. Instrum.* **83** 103705
- [20] Hutter J L and Bechhoefer J 1993 Calibration of atomic-force microscope tips *Rev. Sci. Instrum.* **64** 1868–73
- [21] Proksch R, Schaffer T E, Cleveland J P, Callahan R C and Viani M B 2004 Finite optical spot size and position corrections in thermal spring constant calibration *Nanotechnology* **15** 1344–50
- [22] Bradler S, Schirmeisen A and Roling B 2018 Piezoresponse force and electrochemical strain microscopy in dual AC resonance tracking mode: analysis of tracking errors *J. Appl. Phys.* **123** 035106
- [23] Vasudevan R K, Balke N, Maksymovych P, Jesse S and Kalinin S V 2017 Ferroelectric or non-ferroelectric: why so many materials exhibit “ferroelectricity” on the nanoscale *Appl. Phys. Rev.* **4** 021302
- [24] Balke N, Maksymovych P, Jesse S, Kravchenko I I, Li Q and Kalinin S V 2014 Exploring local electrostatic effects with scanning probe microscopy: implications for piezoresponse force microscopy and triboelectricity *ACS Nano* **10** 10229–36
- [25] MacDonald G A, DelRio F W and Killgore J P 2018 Higher-eigenmode piezoresponse force microscopy: a path towards increased sensitivity and the elimination of electrostatic artifacts *Nano Futures* **2** 015005
- [26] Girard P, Cadet P, Ramonda M, Shmidt N, Usikov A N, Lundin W V, Dunaevskii M S and Titkov A N 2003 Atomic and electrostatic force microscopy observations on gallium nitride *Phys. Stat. Sol. A* **195** 508–15
- [27] Lushta V, Bradler S, Roling B and Schirmeisen A 2017 Correlation between drive amplitude and resonance frequency in electrochemical strain microscopy: influence of electrostatic forces *J. Appl. Phys.* **121** 224302
- [28] Huefner M, Pivonka A, Kim J, Ye C, Blood-Forsythe M A, Zech M and Hoffman J E 2012 Microcantilever Q control via capacitive coupling *Appl. Phys. Lett.* **101** 173110